Author/s:
Li, S-Q;Song, W;Ye, M;Crozier, KB

Title:
Generalized Method of Images and Reflective Color Generation from Ultrathin Multipole Resonators

Date:
2018-06-01

Citation:
Li, S. -Q., Song, W., Ye, M. & Crozier, K. B. (2018). Generalized Method of Images and Reflective Color Generation from Ultrathin Multipole Resonators. ACS PHOTONICS, 5 (6), pp.2374-2383. https://doi.org/10.1021/acsphotonics.8b00161.

Title

Generalized method of images and reflective color generation from ultra-thin multipole resonators

Authors

Shi-Qiang Li,[1]*† Wuzhou Song, [2,3] Ming Ye[1], and Kenneth B. Crozier[1,2]*

Affiliations

1. Department of Electrical and Electronic Engineering, University of Melbourne, VIC 3010 Australia

2. School of Physics, University of Melbourne, VIC 3010 Australia

3. Department of Materials Science and Engineering, Huazhong University of Science and Technology, Wuhan 430030, PR China

*S. Q. Li: mike_li@dsi.a-star.edu.sg ; K. B. Crozier: Kenneth.crozier@unimelb.edu.au

† Present Address: Data Storage Institute, 2 Fusionopolis Way, #08-01 Innovis Tower, Singapore 138634

ABSTRACT

The multipole expansion has found limited applicability for optical dielectric resonators in inhomogeneous environment, such as on the surface of substrates. Here, we generalize the method of images to multipole analysis for light scattering by dielectric nanoparticles on conductive substrates. We present examples illustrating the physical insight provided by our method, including selection rules governing the excitation of the multipoles. We propose and experimentally demonstrate a new mechanism to generate high resolution surface color.

The dielectric resonators employed are very thin (less than 50 nm), i.e. similar in thickness to the plasmonic resonators that are currently being investigated for structural color. The generalized method of images opens up new prospects for design and analysis of metasurfaces and optical dielectric resonators.

KEYWORDS Mie resonance, Structure color, Metasurface, Optical nano-antenna

MAIN TEXT

Optical devices comprising microstructures arranged on a surface to perform an optical function normally achieved with a bulk optical element have a long history, with an early example being the Fresnel zone plate.[1] In recent years, the constituent building blocks of these devices have gone from the micro-scale down to the nano-scale. Concepts from the field of optical metamaterials[2-3]have been adopted and extended, and these devices are now often termed metasurfaces. A key development was the demonstration that planar arrangements of resonant metallic nanostructures could be used to imprint a prescribed phase profile upon a transmitted beam, thereby leading to interesting functionalities such as anomalous refraction[4-5] and vortex beam generation[4]. While many different optical functions have been demonstrated with metallic nanostructures, [6-8] attention has recently turned to dielectrics as the building blocks for metasurfaces, due to significantly lower loss. Dielectric metasurfaces can in general be classified into non-resonant and resonant designs. An example of the non-resonant approach is the work of Schonbrun et al[9], who demonstrated metasurface lenses comprising arrays of silicon nanopillars, whose elliptical cross-sections enabled different phase shifts to be imprinted on the transmitted light depending on the polarization of the incident light. Other non-resonant metasurfaces include circular polarization beam-splitters,[10] holograms and vector beam generators,[11] linear polarization beam-splitter pixels,[12] high numerical aperture lenses,[13] and retro-reflectors.[14]

A challenge of this approach is that the nanopillars need to be relatively tall (on the order of the wavelength divided by the refractive index). By contrast, in the resonant approach, the dielectric building blocks are generally much thinner.[15] In this method, it is the electric dipole (ED) and magnetic dipole (MD, and possibly higher order) resonances[16-17] of dielectric nanoparticles such as nanodisks that control the phase.[18-19] By appropriate design, the ED and MD resonances can occur at the same frequency, allowing the metasurface in principle to have a phase shift of 2π and near-unity transmission.[18, 20-22] The latter results from the ED and MD interfering constructively and destructively in the forward and backward directions, respectively.[23-24] A number of interesting applications of metasurfaces based on resonant dielectric nanoparticles have been demonstrated. Examples include surface-enhanced spectroscopy,[25-26] high resolution color printing,[27-29] magnetic mirrors,[30] non-linear optics,[31] and the ability to generate the Brewster effect with any polarization and at any angle of incidence.[32]

Despite the successes of metasurfaces based on resonant dielectric nanoparticles,[33] an important challenge remains. In the example applications listed above, the dielectric nanoparticles were fabricated on dielectric substrates (or on thick films) with lower refractive indices. In some cases, the nanoparticles were coated with an overlayer whose index matched that of the substrate, with the goal of embedding the nanoparticles in a homogeneous environment.[34] In these situations, the multipole expansion can be readily applied and is very helpful in elucidating the underlying optical physics. Physical interpretation can be much more difficult for highly inhomogeneous environments, e.g. when the resonant dielectric nanoparticle is on a metal substrate.[35-36] The latter is of particular importance for two reasons. First, there are numerous established and potential applications for metal mirrors and for other types of reflective optics[14, 37-40] and the inclusion of resonant dielectric nanoparticles could present interesting new opportunities. Second, the

ability of dielectric metasurfaces to control the propagation and emission of light could be useful in many optoelectronic devices. Such devices however are generally quite inhomogeneous, comprising multiple layers including metals. For these and other reasons, experimental and theoretical studies have recently appeared concerning resonant dielectric above metal films.[37, 41-43] Here, we derive a generalized formulation for multipole analysis of dielectric resonators above a substrate, based on the classical method of images.[44-46] The simplicity of this formulation facilitates physical interpretation and the design of dielectric resonators. As an example, we employ it to demonstrate a new method for structural color patterning at high resolution using silicon resonators that are thinner than 50 nm.

Theoretical Development

The method of images is an established technique for the analysis of electromagnetic fields associated with electrostatic charges and/or dipole radiation near conductive surfaces.[44-45] For example, it simplifies the calculation of radiation from an infinitesimal dipole on a perfect electric conductor (PEC) to the problem of finding a virtual source (image dipole) that accounts for the reflection. The combination of the actual and virtual sources form an equivalent system that gives the same radiated field above the PEC as the actual system. The image dipole generates fields that may interfere constructively or destructively with those generated by the actual source dipole as the direction of the image dipole depends on both the nature of actual source dipole (i.e. whether it is magnetic or electric) and its orientation (e.g. whether it is points vertically or horizontally). The scattering of light from sub-wavelength objects can be approximated as dipole radiation. For nanoparticles with high refractive index and that are too large to be treated in the electrostatic limit, the scattering cross-section may have contributions from modes with orders higher than dipole, such as quadrupoles and octupoles. The method of images thus should be generalized to describe multipoles. To achieve this, we define a new set of multipole coefficients to

describe the scattering behavior of objects on conductive surfaces. We term these the **effective multipole coefficients**:

$$a^{e}_{eff}(l,m) = a^{e}(l,m) - a^{e}(l,-m) \quad (1)$$

$$a^{m}_{eff}(l,m) = a^{m}(l,m) + a^{m}(l,-m) \quad (2)$$

, where $a^{e}(l,m)$ and $a^{m}(l,m)$ are electric and magnetic multipole coefficients calculated by integrating the polarization current ($= \varepsilon_0 \chi_e \boldsymbol{E}$) in the scattering objects, and *l* and *m* are the order and the degree of the multipole under consideration.[47] This approach imposes no restrictions on the shape and orientation of the scatterer. It also imposes no restrictions on the type and direction of the incident wave. A detailed derivation along with some examples is presented in the Supporting Information (SI). The partial scattering cross-section of an order *l* is calculated in the usual way as,

$$C^{e,m}(l) = \frac{\pi}{2k^2} \sum_{m=-l,}^{l} (2l+1) \left| a^{e,m}_{eff}(l,m) \right|^2 \quad (3)$$

, where k ($= \omega/c$) is the wavenumber of the interacting time-harmonic wave. This equation differs from the partial scattering cross-section calculated with the original multipole coefficients only by the factor of 2 in the denominator of the pre-factor, as it is associated with scattering over a hemisphere.

In Figure 1, we show the spectra of the partial scattering cross-sections for the first three orders of *l*, corresponding to dipoles, quadrupoles, and octupoles respectively. Two cases are shown. The first is that of plane wave illumination of a silicon sphere (Figure 1(a)). In the second, a plane wave is normally-incident on a silicon hemisphere on a PEC (Figure 1(b)). The hemisphere of Figure 1(b) has the same radius as the sphere of Figure 1(a). In each case, the total scattering cross-section is also shown, calculated by integrating the Poynting vector associated with the scattered field over a surface enclosing the sphere or

hemisphere. We find that for both cases these total scattering cross-section spectra (blue square markers of Figure 1(a) and (b)) are in complete agreement with spectra consisting of the summation of the first three orders (red thick curves of Figures 1(a) and (b)).

Comparison between the partial scattering cross-sections from the isolated sphere (Figure 1(a)) and those from the hemisphere on the PEC (Figure 1(b)) leads to some interesting observations. First, the magnetic dipole (MD) spectra of the sphere and hemisphere-on-PEC have the same peak positions. It is notable that the magnetic dipole resonant peak position is unaffected by replacing half of the sphere with a PEC. Second, the electric dipole (ED) response vanishes for the hemisphere-on-PEC configuration while the magnetic dipole does not. This is consistent with the original method of images, in which a horizontal source electric dipole is associated with an image electric dipole that is antiparallel with it.[44] Similarly, a horizontal source magnetic dipole is associated with an image magnetic dipole that is parallel with it. Third, the second order resonances, i.e. the electric and magnetic quadrupoles, in the isolated sphere case are completely modified for the hemisphere on PEC case. In particular, the electric quadrupole (EQ) of the hemisphere-on-PEC case has the response of the magnetic octupole (MO) of the isolated sphere. The response of the electric octupole (EO) of the isolated sphere is incorporated in the response of the MD of the hemisphere-on-PEC, broadening the scattering peak that is in the spectral range 800-900 nm. Similarly, the resonance in the spectrum of the magnetic quadrupole (MQ) of the isolated sphere is completely absent in the MQ of the hemisphere-on-PEC case, whose spectrum is rather flat.

This selection and re-ordering of multipoles can be understood from the symmetry of radiation field and the boundary condition on the substrate. For example, the peaks in the spectra of the three modes ED, EQ, and MQ of the free sphere are no longer present in any

of the spectra of the hemisphere-on-PEC case because their field distributions are incompatible with the PEC boundary condition. A closer examination of the EQ of the hemisphere-on-PEC however reveals has a slightly asymmetric line-shape, which we interpret as being due to it retaining some of the response of the EQ of the free sphere. We interpret the incorporation of the EO mode (of the free sphere) into the MD mode (of the hemisphere-on-PEC) as arising from the fact that the original EO mode (of the free sphere) is partially compatible with the boundary condition. This leads to a cancellation of the incompatible components, with the remaining components being incorporated in the MD mode. Further discussions on the conversion and eliminations of octupoles and quadrupoles are provided in the SI (see Figure S-6 and the discussion therein).

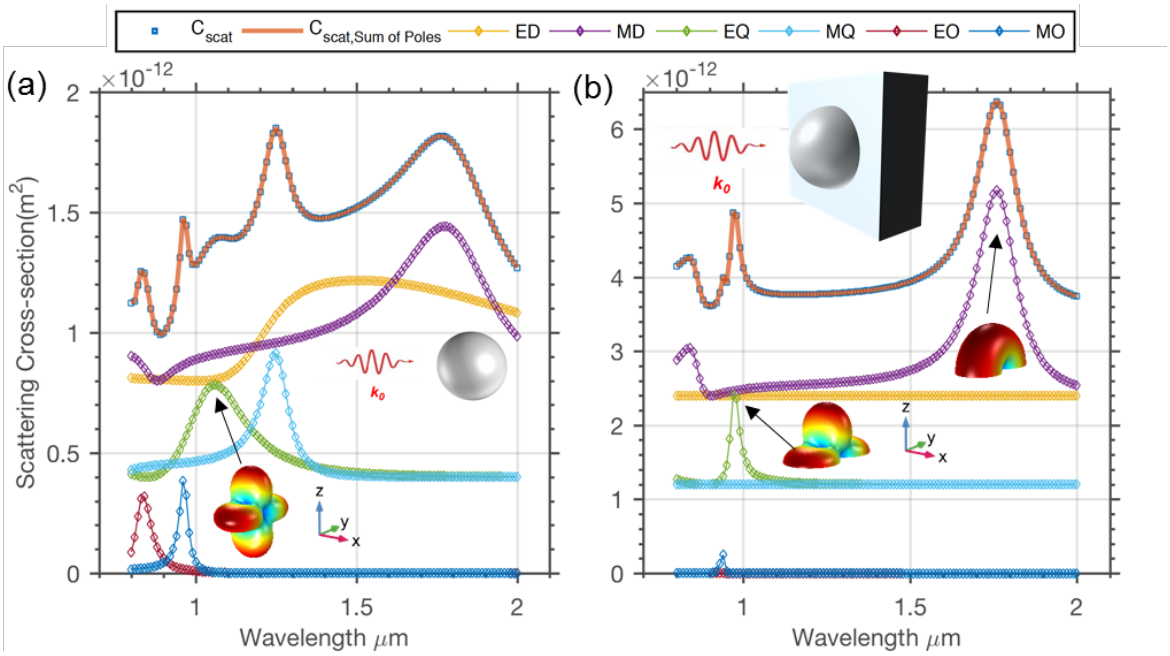

Figure 1. Generalized method of images for multipole scattering by dielectric nanoparticles on conductive substrates. *(a) Partial scattering cross-section spectra of multipolar components for silicon sphere (230 nm radius) with plane wave illumination, as found by integration of polarization current. Scattering cross section (blue square markers) found by integration of Poynting vector associated with scattered fields overlaps perfectly with the summed partial scattering cross-sections of multipoles up to l = 3. Curves have*

been shifted vertically for clarity of presentation (by 4× (3-l)×10^{-13} m^2 for different orders of multipoles and by 1.2×10^{-12} m^2 for C_{scat} and $C_{scat,\ Sum\ of\ Poles}$). Electric dipole, magnetic dipole, electric quadrupole, magnetic quadrupole, electric octupole and magnetic octuopole are denoted ED, MD, EQ, MQ, EO, and MO, respectively. (b) Same as for panel a, except for hemisphere-on-PEC and with partial scattering cross-sections found by generalized method of images (Equations 1-3). Hemisphere has radius of 230 nm. Curves have been shifted vertically for clarity of presentation (by 1.2× (3-l)×10^{-12} m^2 for different orders of multipoles and by 3.6×10^{-12} m^2 for C_{scat} and $C_{scat,\ Sum\ of\ Poles}$). Insets show schematic illustration of illumination of sphere (panel a) and hemisphere (panel b). Insets also show simulated radiation patterns of EQ (panel a), and of EQ and MD (panel b).

The multipole mode selection by PEC transforms a rather rich and broad scattering spectrum (solid blue curve of Figure 1(a)) to one with well-separated peaks (solid blue curve of Figure 1(b)). Indeed, there is a broad wavelength range of low scattering for the hemisphere-on-PEC case. This wavelength range with low scattering for the single hemisphere-on-PEC would result in a wavelength range of high reflectance for an ensemble of hemispheres-on-PEC. This presents a new mechanism for controlling the reflection spectrum of a surface that could be applied in color printing. The color that the surface appears could be readily controlled by appropriate choice of nanoparticle size. This leads to the question of how this method for color printing should be realized in practice. An important consideration is that of manufacturing feasibility. It would be difficult to fabricate an array of silicon hemispheres. Using standard processes however, silicon nanoscale disks and cylinders can be fabricated with excellent control of critical dimensions. It is furthermore known that the resonances supported by such shapes are very similar to those of spheres.[18] Another consideration is what material to use for the substrate, whose response should approximate that of a PEC. We choose aluminum because of its high plasma frequency (i.e. small skin

depth across the entire visible region) and its low cost. In the remainder of this paper, we investigate the optical properties of silicon nano-cylinders and nano-disks on conductive substrates. We consider the scattering of light by silicon nano-cylinders on a PEC using our generalized method of images (Eq. 1 to 3). We then show how this method should be modified when the substrate is not a perfect conductor, but rather a realistic metal. We then analyse the optical properties of silicon nano-disks on an aluminum substrate, and experimentally demonstrate their application to color printing. Note that to be consistent with the literature, in this paper we refer to silicon as a dielectric material to distinguish it from a metal.

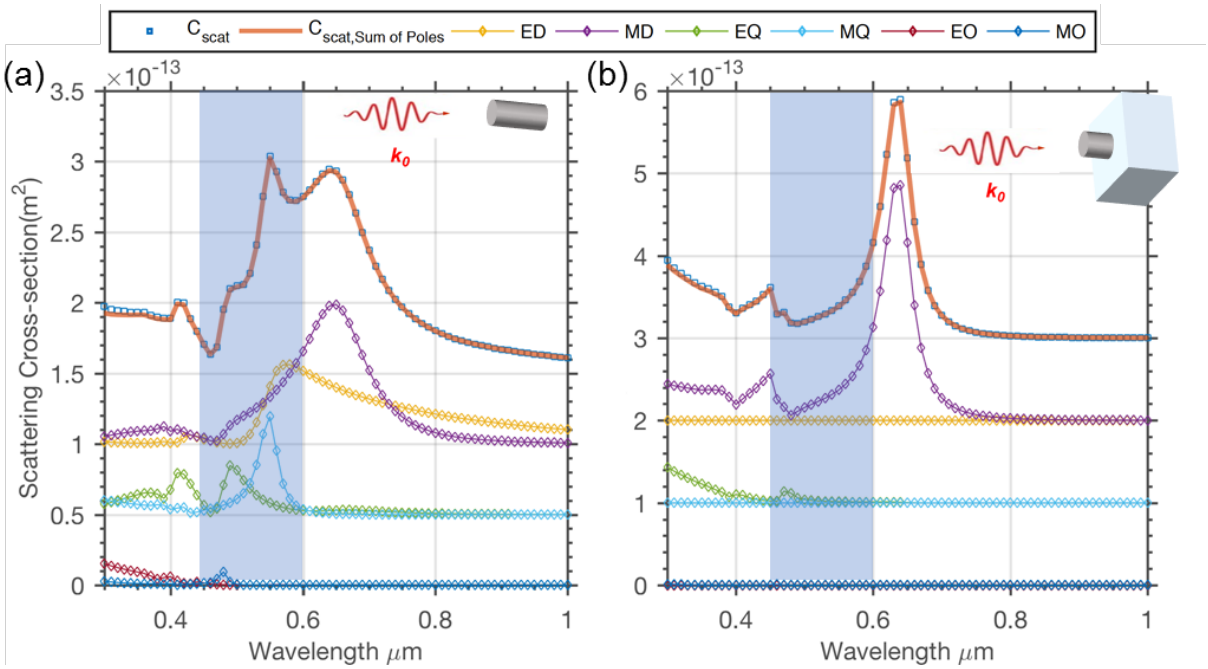

Figure 2. Generalized method of images analysis of light scattering by a dielectric nano-cylinder in free space and on a PEC. *(a). Partial scattering cross-section spectra of multipolar components for silicon nano-cylinder (height: 100 nm, radius: 75 nm) with plane wave illumination. Scattering cross section (blue square markers) found by integration of Poynting vector associated with scattered fields overlaps perfectly with the summed partial scattering cross-sections of multipoles up to l = 3. Curves have been shifted vertically for*

clarity of presentation (by 5× (3-l)×10^{-14} m^2 for different orders of multipoles and by 1.5×10^{-13} m^2 for C_{scat} and $C_{scat,\ Sum\ of\ Poles}$). (b). Partial scattering cross-section spectra of effective multipolar components for silicon nano-cylinder (height: 50 nm, radius: 75 nm) on PEC, with plane wave illumination. Total scattering cross section spectrum shown as blue markers. The summation of partial scattering cross-sections up to l = 3 is shown as the thick red line. Curves have been shifted vertically for clarity of presentation (by (3-l)×10^{-13} m^2 for different orders of multipoles and by 10^{-13} m^2 for C_{scat} and $C_{scat,\ Sum\ of\ Poles}$). By comparison between the blue-shaded regions in (a) and (b), it can be seen that in (b) this region has low scattering, a result of multipoles being eliminated or suppressed when the half-rod is placed on the PEC.

We now apply our generalized method of images to the analysis of a silicon nano-cylinder in free space (Figure 2(a)). It can be seen that the first three orders of multipole resonances are sufficient to account for total scattering cross section in the visible region (400 nm to 700 nm). The strengths of the resonances decrease with order. We next analyze light scattering by a silicon nano-cylinder on a PEC (Figure 2(b)), whose height is half that of the nano-cylinder in free space of Figure 2(a)). It can be seen that the suppression of the quadrupole resonances and electric dipole resonances creates a spectral region with low scattering, which is indicated with blue shading in Figure 2. This region is ~150 nm wide, and offers interesting possibilities for reflected color.

To apply our generalized method of images at visible wavelengths, we must take into account the fact that metals are not PECs in this spectral range. Real metals have finite and complex refractive indices, with the latter resulting in absorption of the fields created by the multipoles. To model this appropriately, we introduce a parameter called image strength, denoted by Γ, to modify Eqn. (1) and (2). We choose Γ to denote image strength because it

is conceptually related to reflection. We note however that it is not the same as the reflection coefficient for a plane wave at the interface between two media, which is sometimes referred to by the same symbol. These equations thus become

$$a^{e}_{eff}(l,m) = a^{e}(l,m) - \Gamma a^{e}(1,-m) \quad (4)$$

$$a^{m}_{eff}(l,m) = a^{m}(l,m) + \Gamma a^{m}(1,-m) \quad (5)$$

, where $\Gamma = \dfrac{\varepsilon_s - \varepsilon_1}{\varepsilon_s + \varepsilon_1}$, and ε_s and ε_1 are the permittivities of the substrate and of the surrounding region (e.g. air). Further discussion on image strength is provided in SI.

Experimental

We now describe our experimental realization of color printing with dielectric resonators on conductive substrates. We begin by considering the optical properties of silicon nano-disks on aluminum substrates by simulations and experiments. In these simulations, the complex refractive index for aluminum is taken from the compilation of Palik[48], while that for silicon is based on the values we measure experimentally by ellipsometry (Figure 3(a)). This plot also includes the complex refractive index of amorphous silicon from the literature.[49] We observe that the real (n) and imaginary (k) parts of the refractive index of the silicon we deposit by electron-beam evaporation (EBE) are much smaller than those of the reference value for amorphous silicon. We attribute the reduced indices to be the result of our film having a low packing density. The importance of sample preparation upon the optical properties of amorphous silicon was recognized by Pierce and Spicer.[49] In Figure 3(b), we plot the partial scattering cross sections of the EQ and MD modes of the silicon nano-disk on aluminum, calculated using our generalized method of images (Equations 4-5). The total scattering cross section is also shown. The MD resonance of Figure 3(b) is

broader than it would be, had we employed the optical properties of a-Si as reported by Pierce and Spicer rather than those of our EBE-deposited material. It can be seen nonetheless that the total scattering cross section (Figure 3(b)) displays a pronounced trough between the resonant peaks of the MD and EQ. This is created by the conductive substrate eliminating the ED, and modifying the nature of the EQ and MQ modes. The radiation patterns at the wavelengths of $\lambda = 380\ nm$ and $660\ nm$ are plotted in the inset. The pattern at $\lambda = 380\ nm$ is consistent with the upper half of the four-lobed pattern that one would expect for electric quadrupoles (*l = 2, m = ±1*). The bottom half of the pattern one would expect for an electric quadrupole is of course absent due to the presence of the conductive substrate. Similarly, the pattern at $\lambda = 660\ nm$ has a half-donut shape, which is consistent with it being the upper half of the donut pattern that one would expect for magnetic dipoles (*l =1, m = ±1*), shown as the inset in Figure 1(b). It can also be seen that the radiation intensity along the surface is small compared to that occurring in Figure 1(b). This is due to resistive losses in the aluminum that occur when propagation is along the surface.

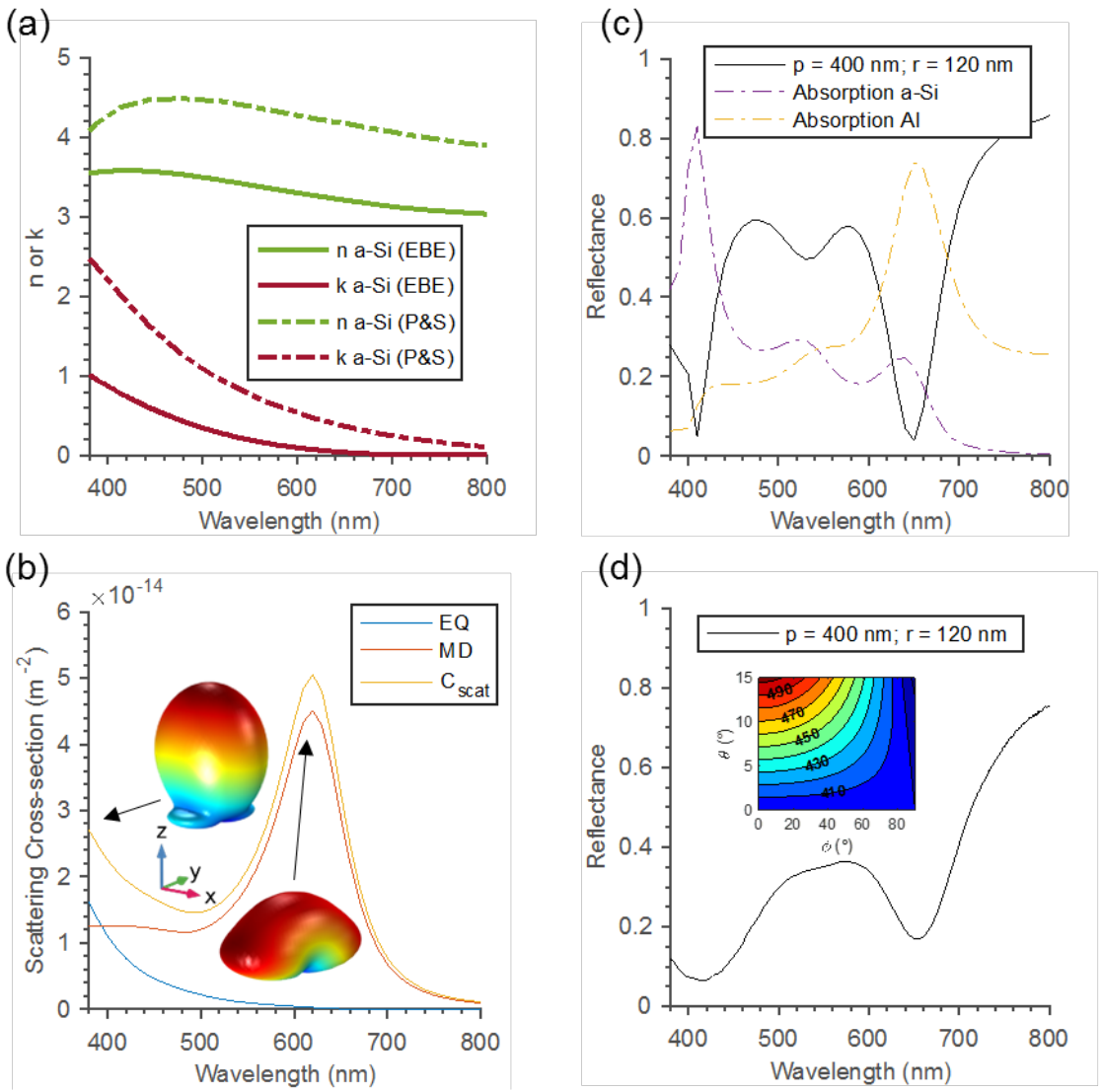

Figure 3. Optical properties of silicon nano-disks on aluminum substrates: simulations and experiments. *(a). Complex refractive indices vs wavelength of amorphous silicon, as measured experimentally for films we deposit by electron beam evaporation (a-Si (EBE)) and as previously reported in the literature (a-Si (P&S)).*[49] *(b) Partial scattering cross-section spectra of electric quadrupole and magnetic dipole terms for isolated silicon nano-disk on aluminum. Total scattering cross section (C_{sca}) is also shown. Radiation patterns that occur at peaks in scattering cross section spectra are also plotted, with the orientation of the coordinate axes (xyz) as shown. Illumination is from a plane wave propagating along the z axis (-z direction), whose electric field is along the y axis. (c). Simulated reflectance*

spectrum (black curve) of square array (period 400 nm) of silicon nano-disks (radius 120 nm and height 45 nm) on an aluminum substrate. Absorption within silicon and within aluminum vs wavelength are plotted as purple and yellow curves, respectively. (d) Experimentally measured reflectance spectrum of square array (period 400 nm) of silicon nano-disks (radius 120 nm) on aluminum. Inset: calculated wavelength at which first diffraction order transitions from evanescent to propagating, as a function of azimuthal φ and elevation θ angles of incident plane wave.

We now consider the case in which the silicon nano-disks are formed in an array. The reflection spectrum simulated for a square array (period 400 nm) of silicon nano-disks (radius 120 nm, height 45 nm) on an aluminum substrate is shown as Figure 3(c). It can be seen that there are dips in the reflectance at wavelengths of $\lambda \approx 410\,nm$ and $650\,nm$. It can also be seen that these dips are associated with peaks in the absorption spectra of the silicon nano-disks (purple curve) and of the aluminum (yellow curve), which are also plotted in Figure 3(c). As we describe in further detail below, we fabricate an array of silicon disks on an aluminum substrate. We measure the reflection spectrum of this sample (Figure 3(d)). It can be seen that the experimentally-measured spectrum (Figure 3(d)) exhibits dips whose positions are very close to the predictions of simulations (Figure 3(c)). There are some differences between the spectra however. In experiments, the longer-wavelength dip has a minimum reflectance value of ~0.17, while simulations predict ~0.04. For the spectral region between the dip features, the measured reflectance is smaller than the predictions of simulations. These differences may be in part due to the fact that the simulations are performed for normal incidence illumination, while in the experiments a microscope objective with a numerical aperture (NA) of 0.3 is used (Nikon CFI Plan Fluor 10 X Objective). This NA corresponds to an illumination angle, i.e. elevation angle θ, of up to 17°. The reflection spectrum is expected to be dependent on the angle of illumination for

two reasons. First, the optical response of an isolated silicon nano-disk (on aluminum) will in general vary with angle of incidence. Second, for a silicon nano-disk array, interactions between nano-disks play an important role in the optical response. These interactions are dependent on the angle of incidence. As an example, consider the wavelength at which light near normal incidence on the array is coupled into a diffraction order that runs along the plane of the substrate. This leads to a pronounced interaction between nanoparticles and has also been termed the "lowest order lattice resonance". As shown in the inset of Figure 3(d), this wavelength varies with the elevation and azimuthal angles of the incident light. It matches the array period (400 nm) at normal incidence, and is larger at other angles. In addition to the angle of illumination, the differences between simulation and experiment can be attributed to surface roughness of the aluminum surface (~6 nm, as determined by atomic force microscopy).

Further insight into the optical response of the silicon nano-disk array can be obtained by considering the field distributions that occur at the wavelengths of the dips of the reflection spectrum (Figure 3(c)). As discussed above, at these wavelengths ($\lambda = 410\,nm$ and $650\,nm$), the absorption spectra of the silicon nano-disk and of the aluminum film exhibit peaks. We plot the scattered field distributions at these wavelengths in Figure 4. It can be seen that for illumination at $\lambda = 410\,nm$, the field peaks at the corners of the disks (Figure 4(a)). Though it is a little difficult to see from Figure 4(a) due to the very strong fields at the corners, the field is also appreciable inside the disks, which results in absorption. These field patterns are consistent with quadrupole resonances. These resonances are enhanced due to the lattice resonance occurring at around the same spectral position ($\lambda = 400\,nm$). For illumination at $\lambda = 650\,nm$, it can be seen that the field at the boundary between the nano-disk and the

aluminum substrate is appreciable (Figure 4(b)). This is consistent with the resonance producing a peak in the absorption spectrum of the aluminum substrate (Figure 3(c)).

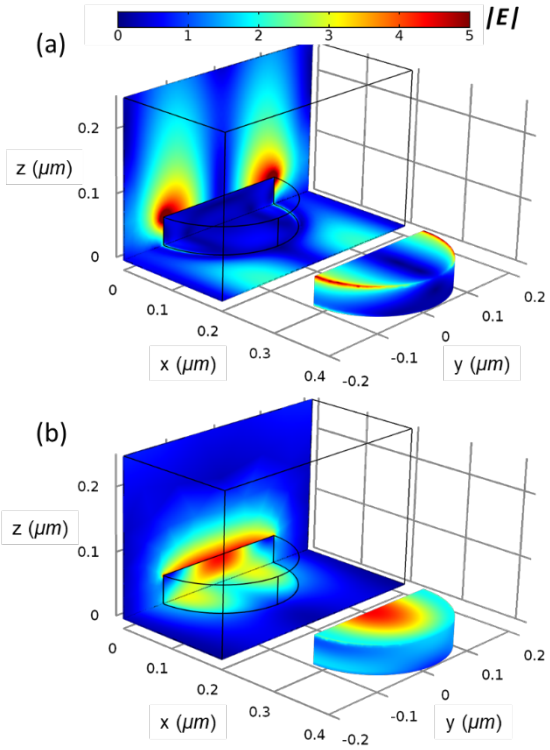

Figure 4. ***Simulated scattered electric field strength distribution.*** *(a) shows the field strength distribution of the silicon nano-disk array (on Al) illuminated at a wavelength of 410 nm. Only half of the cell is shown and the half disk is displaced from its original position to reveal the field inside. The field strength distribution for illumination at a wavelength of 650 nm is shown in (b).*

We now describe the fabrication method for the silicon nanodisk array on aluminum. Key steps are shown in Figure 5(a). Fabrication starts with a silicon wafer (4 inch, (100) orientation) onto which aluminum (100 nm) and then amorphous silicon (50 nm) films are deposited by e-beam evaporation (EBE). The wafer is then diced with a wafer saw into square samples (15 mm side length). E-beam resist (ZEP520A, Zeon Chemicals) is then spun onto the sample which is then baked, exposed using standard e-beam lithography

(EBPG5000plusES, Vistec), and developed. These steps result in an array of disks in the resist, which is transferred to the underlying silicon by inductively-coupled reactive ion etching using SF_6 and C_4F_8 gases (Plasmalab100 ICP380, Oxford Instruments). The resist is then removed by soaking the sample in ZDMAC remover (Zeon Chemicals) for 5 minutes followed by rinsing with iso-propanol. A scanning electron microscope (SEM) image of one of the finished arrays is shown as Figure 5(b). The disks in this array have radii of 90 nm (design value of e-beam lithography step) and are in square arrays of period 300 nm. Atomic force microscopy (Figure 5(c)) confirms that the disks have heights of ~ 50 nm.

A bright-field optical microscope image of ten disk arrays is shown as Figure 5(d). This image is obtained with illumination from a tungsten lamp with the same objective lens for spectrum collection (NA = 0.3). Each array consists of a square lattice of silicon nano-disks, whose radii range from 75 to 150 nm. The larger arrays have overall extents of 200 by $200\ \mu m$, and the smaller arrays are 150 by $150\ \mu m$. To maintain the filling fraction, the array periods vary from 250 to 500 nm. Let us begin by considering the color exhibited by the larger arrays (200 by $200\ \mu m$). As the nano-disk radius increases, the arrays vary in color from blue to green, yellow and orange. Our physical interpretation of the observed color is as follows. As discussed in relation to Figure 3(c), a band of high reflectance occurs for the spectral region between the EQ and MD resonances. As the disk radius is increased, the resonances (and therefore the high reflectance band) shift from shorter to longer wavelengths. This results in the color change that is observed in Figure 5(d). We now consider the two smaller arrays that contain the smallest radius disks (bottom two arrays of Figure 5(d)). For these arrays, the observed color is a combination of this band of high reflectance (between the EQ and MD) and the high reflectance that occurs on the longer-wavelength side of the MD resonance.

Dark-field optical microscopy has been previously used to measure scattering spectra from arrays of silicon nanoparticles on glass substrates,[27] with the scattering occurring into the diffraction orders. Our silicon nanodisks are not isolated, but are fabricated in square arrays with periods (p) of 500 nm and below. We expect that for only wavelengths shorter than $\lambda = 2p \times NA$ could a non-zero diffraction order be excited from an array and collected by the lens. In other words, for longer wavelengths, the reflected field can be thought of as specular and free from higher diffraction orders. A dark-field microscope image of the arrays is shown as Figure 5(e). This image is obtained with Nikon Eclipse microscope with an objective lens of $NA = 0.3$. For wavelengths longer than 250 nm, therefore, only specular reflection is expected from the nanowire arrays. One would expect this specularly-reflected light to exhibit color. This specularly-reflected light should not be collected by our microscope as it is a dark-field design. It can be seen however that the nanowire arrays appear brighter than their surroundings in the dark-field images of Figure 5(e). We attribute this to scattering from surface roughness and other fabrication imperfections. It is also notable that the color variation from one array to the next is much less pronounced than for the bright-field images (Figure 5(d)), which is consistent with our expectations.

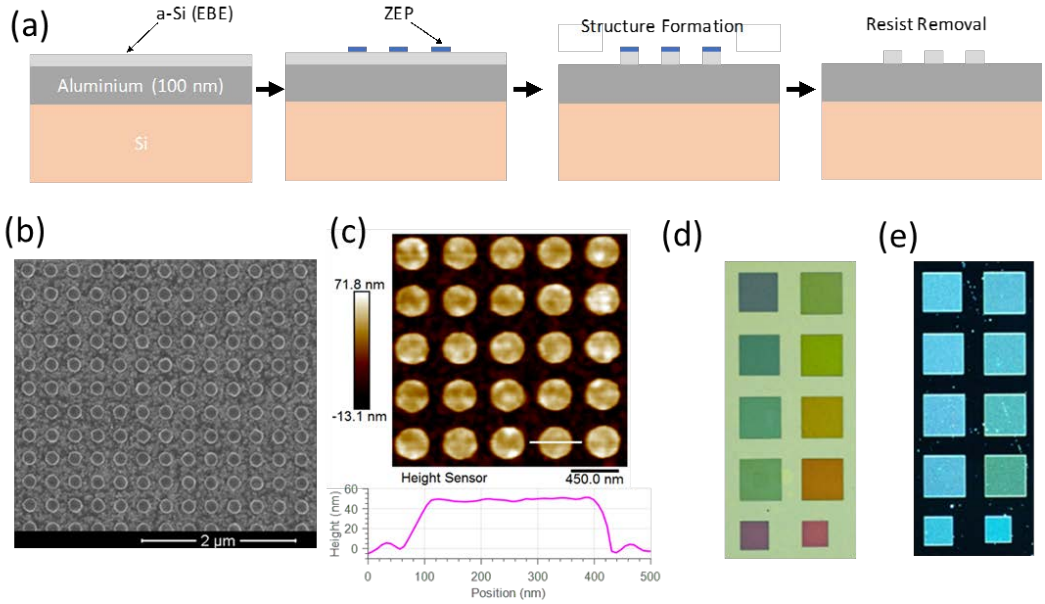

Figure 5. Experimental demonstration of color printing using silicon nano-disks on an aluminum substrate. *(a) Schematic diagram of fabrication process. (b). Top view scanning electron microscope (SEM) image of array (radius = 90 nm; period = 300 nm). (c) Atomic force microscope (AFM) image of Si nanodisk array (radius = 135 nm; period = 450 nm), from which disk height is determined. (d). Bright-field optical microscope image of fabricated arrays. Array periods are 275, 375, 350, 325, 300, 400, 425, 450, 500, and 250 nm, clockwise from bottom left. In same sequence, the radii are 83, 113, 105, 98, 90, 120, 128, 135, 150, and 75 nm. (e). Dark field optical microscope image of sample also shown as panel d.*

We next fabricate additional samples, this time with a silicon thickness of 45 nm. In Figure 6(a), we present the reflection spectra measured from ten arrays of silicon nano-disks. The nano-disks cover the same range of radii (75 to 150 nm) and periods (250 to 500 nm) as the arrays with heights of 50 nm (Figure 5). The measured reflection spectra are shown as Figure 6(a), with the curves plotted with vertical offsets that increase with nanodisk radius. We also show bright-microscope images of the arrays that are obtained with the same microscope (and lighting conditions) that is used for Figure 5(d). These images are plotted on the right hand side of Figure 6(b). It can be seen that the color of the background region (45 nm thick unpatterned Si film on Al), is now light blue, i.e. differing from the green color of the 50 nm thick Si film on aluminum (Figure 5(d)). The resonance positions of the arrays are also blue-shifted, now that the disk height is decreased. For example, the array comprising 90 nm radius disks on a 300 nm period is now purplish, unlike the blue color of the corresponding array of Figure 5(d). In Figure 6(b), we present the reflection spectra simulated for the arrays. These are in reasonable agreement with the experiments, showing a pair of dips that shift to longer wavelengths as the nano-disk radius is increased. For the array containing the nano-disks with the largest radii (150 nm), for example, the measured spectrum shows dips at ~510 nm and ~705 nm. The corresponding simulated spectrum has dips at ~500 nm and ~710 nm. As before (Figure 3(c) and (d)), there are differences between simulation and experiment however. The key differences are that the simulated spectra show

an additional dip between the pair of dips discussed above, and dips are deeper (i.e. lower reflectance at the dip center). As before, we attribute these differences to the illumination not being at purely normal incidence in experiments, and to non-idealities (e.g. surface roughness of silicon and aluminum) in fabricated samples.

As a further demonstration of color printing, we realize the logo of our institution using small arrays of nano-disks with different radii and periods (Figure 6(c)). The outline of the shield behind the goddess figure, the name of the institution and the outline of the ribbon (containing the institutional motto in Latin) exhibit a blue color that is produced using arrays of nano-disks with radii of $r = 90\ nm$ on a period of $p = 300\ nm$. The pink color of the clothes and wings of the goddess is achieved using arrays of nano-disks with $r = 83\ nm$ and $p = 275\ nm$. The leaves held by the goddess have a green color, achieved using a nano-disk array with $r = 105\ nm$ and $p = 350\ nm$. To give it a yellow tone, the skin is colored with a nano-disk array with $r = 135\ nm$ and $p = 450\ nm$. The stars underneath the leaves are orange, achieved with nano-disk arrays with $r = 150\ nm$ and $= 500\ nm$. The letters 'POSTERA CRESCAM LAUDE' and the hair of the goddess have a dark appearance, achieved by combining disks with different radii (75 nm, 90 nm, and 105 nm).

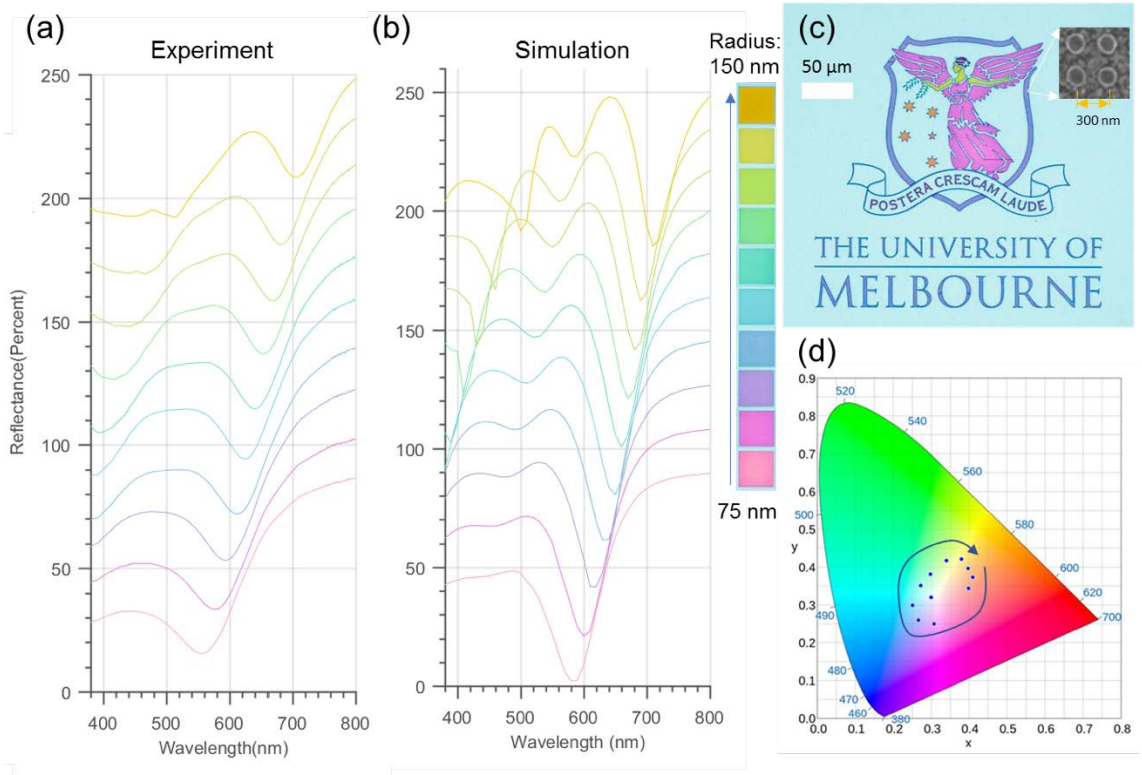

Figure 6. Optical characterisation of color printing using silicon nanodisks on aluminum substrate. *(a) Reflectance spectra measured from arrays of silicon disks on an aluminum substrate. Inset is bright-field optical microscope image of arrays. Line color used for plotting spectrum of each array is chosen to match color that the array appears in optical microscope image. Successive spectra are shifted vertically by 15% per spectrum for clarity of presentation. (b). Reflectance spectra simulated for arrays with same parameters as those of panel a, using same color coding and vertical offset schemes. (c) Optical microscope image of demonstration of color printing of institutional logo of authors of this paper. Surrounding region (light blue color) consists of unpatterned silicon film on aluminum. (d). Positions (black dots) of measured reflectance spectra plotted in CIE 1931 chromaticity chart. Arrays increase in period as indicated by direction of arrow, in same manner as arrowed line of panel a.*

The spectra generated by the ten arrays of Figure 6(a) are converted to color and plotted as ten color coordinates in a standard CIE 1931 chromaticity chart as Figure 6(d). The illuminant used in this conversion is the standard D65 light source. The trajectory made by the color coordinates of the arrays with increasing nano-disk radius is a clockwise path, from red to blue to green to orange.

The results presented thus far are for periodic arrays of nano-disks. This leads to the question of the influence of the nano-disk arrangement upon the reflection spectrum (and therefore the color). To address this, we fabricate nano-disks in randomized arrangements at different densities. The reflection spectra measured from these devices are presented in the SI. We find that for devices with nano-disks of the same radius, the positions of the spectral dips vary with nano-disk density (as would be inevitable due to near-field coupling), but not very substantially. Earlier in this paper, we interpreted the shorter-wavelength dip as being associated with the EQ mode. As for some arrays this occurs at a wavelength similar to the array period, one wonders about the possible contribution of the lattice resonance. The results we obtain from the randomized devices confirm the importance of the EQ mode, as for these devices the shorter-wavelength dip occurs despite the absence of the lattice resonance. Optical microscope images of the devices are also presented in the SI. We find that for devices containing nano-disks with the same radius, the lower density devices have less saturated color, which could be useful in color printing.

Discussion

In this work, we propose a generalization of the method of images to allow it to be applied to the multipole expansion for dielectric nanoparticles on conductive surfaces. We anticipate that our method will enable useful physical insight into the scattering of light in this

configuration, showing how the process can be described in a compact fashion by what we term the effective multipole coefficients. Our method furthermore reveals the selection rules that govern the excitation of the multipole resonances, thereby explaining which excitations are naturally forbidden by symmetry. We show how our method can be applied to real metals with loss via the concept of image strength. Lastly, we apply our method to experimentally demonstrate a new mechanism for color printing, in which silicon nano-disks are formed on an aluminum substrate. We show that we can shift a spectral band of high reflectance across the visible spectrum by appropriate choice of nano-disk radius, thereby achieving a range of colors. This high reflectance band occurs between the spectral positions of the electric quadrupole (EQ) and magnetic dipole (MD) mode resonances. As revealed by our generalized method of images, there are other modes such as the electric dipole that would occur in this spectral range that are not excited due to symmetry considerations.

Materials and Methods

Simulation of Isolated particle. The simulation of isolated particle on metallic substrate (such as aluminum) is performed with the model setup provided by COMSOL Inc. (Model Application ID: 14699). https://www.comsol.com/model/scatterer-on-substrate-14699 (accessed on March 12, 2018).

Calculation of Original Multipole Coefficients. First, an FEM simulation of isolated silicon sphere illuminated by a plane wave is performed, and we thus obtain the electric field in the silicon sphere. We subsequently perform integration according to the formulation described Grahn et al.[47] The calculation of the spherical multipole coefficients of the silicon sphere. The setup of our model follows that from COMSOL Inc. (Model Application ID: 31901).

https://www.comsol.com/model/multipole-analysis-of-electromagnetic-scattering-31901 (accessed on March 12, 2018)

Calculation of Effective Multipole Coefficients. First, the multipole coefficients are found for the particle on substrate, with the origin of integration set to be at the center of the particle. Following that, Eqn. (1) and (2) are used to calculate the effective multipole coefficients.

Simulation of periodic arrays of silicon nanodisk. FEM simulations with periodic boundary conditions are performed to obtain the reflectance spectra and near field profiles. A reference model can be found on COMSOL website. (Model Application ID: 14704) https://www.comsol.com/model/plasmonic-wire-grating-wave-optics-14705 (accessed on March 12, 2018)

Fabrication of silicon nano-disks on aluminum film. The fabrication process is described in detail in Figure 5 and the associated text.

Refractive index determination. The refractive index of a-Si (EBE) is measured on a sample with 300 nm a-Si deposited using the same conditions as used for the nanodisk samples using an ellipsometer (J.A. Woollam M2000-DI).

Height Characterization. Height measurement is carried out on a commercial Atomic Force Microscope (Dimension Icon, Bruker) using a NanoScope V controller. The microscope is operated at tapping mode using FESP-V2 tip (Bruker) with resonant frequency at around 75 kHz. The typical line scan rate is 1 Hz during the measurements.

Supporting Information

Fig. S1. Concept and numerical results of dipolar mode of a particle scattering on PEC.

Fig. S2. Comparison between effectively multipole expansions and the original multipole expansion of light scattering by an arbitrary particle on PEC by tilted incident light.

Fig. S3. Numerical results of effective multipole expansions on different conductive substrates.

Fig. S4. AFM images of periodic and randomized silicon particle arrays.

Fig. S5. Spectra and optical images of arrays with different densities.

Fig. S6. Schematics of multipole mode selection and transformation.

Acknowledgments

This work was supported by the Australian Research Council (DP150103736 and FT140100577) and by the Victorian Endowment for Science, Knowledge and Innovation (VESKI). Fabrication work was performed at the Melbourne Centre for Nanofabrication (MCN) in the Victorian Node of the Australian National Fabrication Facility (ANFF).

S.Q.L and K.B.C. developed the concept. S.Q.L devised the theory, performed fabrication, experiments, simulation and data analysis. S.Q.L., W.S., M. Y, and K.B.C. discussed the results. S.Q.L. and K.B.C. wrote the manuscript.

References

(1) Lipson, A.; Lipson, S. G.; Lipson, H., *Optical physics*. Cambridge University Press: 2010.
(2) Lezec, H. J.; Dionne, J. A.; Atwater, H. A., *Science* **2007,** *316* (5823), 430-432.
(3) Shalaev, V. M., *Nature photonics* **2007,** *1* (1), 41-48.
(4) Yu, N.; Genevet, P.; Kats, M. A.; Aieta, F.; Tetienne, J.-P.; Capasso, F.; Gaburro, Z., *Science* **2011,** *334* (6054), 333-337.
(5) Ni, X.; Emani, N. K.; Kildishev, A. V.; Boltasseva, A.; Shalaev, V. M., *Science* **2012,** *335* (6067), 427-427.
(6) Yu, N.; Capasso, F., *Nature Materials* **2014,** *13* (2), 139.
(7) Kildishev, A. V.; Boltasseva, A.; Shalaev, V. M., *Science* **2013,** *339* (6125), 1232009.
(8) Duan, X.; Kamin, S.; Liu, N., *Nature Communications* **2017,** *8*, 14606.
(9) Schonbrun, E.; Seo, K.; Crozier, K. B., *Nano Letters* **2011,** *11* (10), 4299-4303.

(10) Khorasaninejad, M.; Crozier, K. B., *Nature communications* **2014,** *5*, 5386.
(11) Arbabi, A.; Horie, Y.; Bagheri, M.; Faraon, A., *Nature Nanotechnology* **2015,** *10* (11), 937-943.
(12) Khorasaninejad, M.; Zhu, W.; Crozier, K., *Optica* **2015,** *2* (4), 376-382.
(13) Khorasaninejad, M.; Chen, W. T.; Devlin, R. C.; Oh, J.; Zhu, A. Y.; Capasso, F., *Science* **2016,** *352* (6290), 1190-1194.
(14) Arbabi, A.; Arbabi, E.; Horie, Y.; Kamali, S. M.; Faraon, A., *Nature Photonics* **2017,** *11*, 415-420.
(15) Lin, D.; Fan, P.; Hasman, E.; Brongersma, M. L., *Science* **2014,** *345* (6194), 298-302.
(16) Evlyukhin, A. B.; Novikov, S. M.; Zywietz, U.; Eriksen, R. L.; Reinhardt, C.; Bozhevolnyi, S. I.; Chichkov, B. N., *Nano Letters* **2012,** *12* (7), 3749-3755.
(17) Kuznetsov, A. I.; Miroshnichenko, A. E.; Fu, Y. H.; Zhang, J.; Luk'yanchuk, B., *Scientific Reports* **2012,** *2*, 492.
(18) Decker, M.; Staude, I.; Falkner, M.; Dominguez, J.; Neshev, D. N.; Brener, I.; Pertsch, T.; Kivshar, Y. S., *Advanced Optical Materials* **2015,** *3* (6), 813-820.
(19) Kuznetsov, A. I.; Miroshnichenko, A. E.; Brongersma, M. L.; Kivshar, Y. S.; Luk'yanchuk, B., *Science* **2016,** *354* (6314), 2472.
(20) Yu, Y. F.; Zhu, A. Y.; Paniagua-Domínguez, R.; Fu, Y. H.; Luk'yanchuk, B.; Kuznetsov, A. I., *Laser & Photonics Reviews* **2015,** *9* (4), 412-418.
(21) Campione, S.; Basilio, L. I.; Warne, L. K.; Sinclair, M. B., *Optics Express* **2015,** *23* (3), 2293-2307.
(22) Liu, S.; Vaskin, A.; Campione, S.; Wolf, O.; Sinclair, M. B.; Reno, J.; Keeler, G. A.; Staude, I.; Brener, I., *Nano letters* **2017,** *17* (7), 4297-4303.
(23) Fu, Y. H.; Kuznetsov, A. I.; Miroshnichenko, A. E.; Yu, Y. F.; Luk'yanchuk, B., *Nature Communications* **2013,** *4*, 1527.
(24) Person, S.; Jain, M.; Lapin, Z.; Sáenz, J. J.; Wicks, G.; Novotny, L., *Nano Letters* **2013,** *13* (4), 1806-1809.
(25) Albella, P.; Alcaraz de la Osa, R.; Moreno, F.; Maier, S. A., *ACS Photonics* **2014,** *1* (6), 524-529.
(26) Caldarola, M.; Albella, P.; Cortés, E.; Rahmani, M.; Roschuk, T.; Grinblat, G.; Oulton, R. F.; Bragas, A. V.; Maier, S. A., *Nature Communications* **2015,** *6*.
(27) Proust, J.; Bedu, F. d. r.; Gallas, B.; Ozerov, I.; Bonod, N., *ACS Nano* **2016,** *10* (8), 7761-7767.
(28) Liu, Z.; Du, S.; Cui, A.; Li, Z.; Fan, Y.; Chen, S.; Li, W.; Li, J.; Gu, C., *Advanced Materials* **2017**.
(29) Dong, Z.; Ho, J.; Yu, Y. F.; Fu, Y. H.; Paniagua-Dominguez, R. n.; Wang, S.; Kuznetsov, A. I.; Yang, J. K. W., *Nano letters* **2017,** *17* (12), 7620-7628.
(30) Liu, S.; Sinclair, M. B.; Mahony, T. S.; Jun, Y. C.; Campione, S.; Ginn, J.; Bender, D. A.; Wendt, J. R.; Ihlefeld, J. F.; Clem, P. G., *Optica* **2014,** *1* (4), 250-256.
(31) Shcherbakov, M. R.; Neshev, D. N.; Hopkins, B.; Shorokhov, A. S.; Staude, I.; Melik-Gaykazyan, E. V.; Decker, M.; Ezhov, A. A.; Miroshnichenko, A. E.; Brener, I., *Nano Letters* **2014,** *14* (11), 6488-6492.
(32) Paniagua-Domínguez, R.; Yu, Y. F.; Miroshnichenko, A. E.; Krivitsky, L. A.; Fu, Y. H.; Valuckas, V.; Gonzaga, L.; Toh, Y. T.; Kay, A. Y. S.; Luk'yanchuk, B., *Nature Communications* **2016,** *7*.
(33) Khorasaninejad, M.; Capasso, F., *Science* **2017,** *358* (6367), eaam8100.
(34) Staude, I.; Miroshnichenko, A. E.; Decker, M.; Fofang, N. T.; Liu, S.; Gonzales, E.; Dominguez, J.; Luk, T. S.; Neshev, D. N.; Brener, I., *ACS Nano* **2013,** *7* (9), 7824-7832.
(35) Evlyukhin, A. B.; Reinhardt, C.; Evlyukhin, E.; Chichkov, B. N., *JOSA B* **2013,** *30* (10), 2589-2598.

(36) Hutter, T.; Huang, F. M.; Elliott, S. R.; Mahajan, S., *The Journal of Physical Chemistry C* **2013,** *117* (15), 7784-7790.
(37) Sinev, I.; Iorsh, I.; Bogdanov, A.; Permyakov, D.; Komissarenko, F.; Mukhin, I.; Samusev, A.; Valuckas, V.; Kuznetsov, A. I.; Luk'yanchuk, B. S., *Laser & Photonics Reviews* **2016,** *10* (5), 799-806.
(38) Zhang, S.; Kim, M.-H.; Aieta, F.; She, A.; Mansuripur, T.; Gabay, I.; Khorasaninejad, M.; Rousso, D.; Wang, X.; Troccoli, M., *Optics Express* **2016,** *24* (16), 18024-18034.
(39) Flauraud, V.; Reyes, M.; Paniagua-Dominguez, R.; Kuznetsov, A. I.; Brugger, J., *ACS Photonics* **2017**.
(40) Glybovski, S. B.; Tretyakov, S. A.; Belov, P. A.; Kivshar, Y. S.; Simovski, C. R., *Physics Reports* **2016,** *634*, 1-72.
(41) Li, H.; Xu, Y.; Xiang, J.; Li, X.; Zhang, C.; Tie, S.; Lan, S., *Nanoscale* **2016,** *8* (45), 18963-18971.
(42) Zhang, S.; Xu, H., *ACS Nano* **2012,** *6* (9), 8128-8135.
(43) Holsteen, A. L.; Raza, S.; Fan, P.; Kik, P. G.; Brongersma, M. L., *Science* **2017,** *358* (6369), 1407-1410.
(44) Balanis, C. A., *Advanced engineering electromagnetics*. John Wiley & Sons: 1999.
(45) Novotny, L.; Hecht, B., *Principles of nano-optics*. Cambridge university press: 2012.
(46) Campione, S.; Warne, L. K.; Langston, W. L.; Basilio, L. I., *Progress In Electromagnetics Research* **2018,** *82*, 1-11.
(47) Grahn, P.; Shevchenko, A.; Kaivola, M., *New Journal of Physics* **2012,** *14* (9), 093033.
(48) Palik, E. D., *Handbook of optical constants of solids*. Academic press: 1998; Vol. 3.
(49) Pierce, D. T.; Spicer, W. E., *Physical Review B* **1972,** *5* (8), 3017.

For Table of Contents Use Only

Title

Generalized method of images and reflective color generation from ultra-thin multipole resonators

Authors

Shi-Qiang Li, Wuzhou Song, Ming Ye, and Kenneth B. Crozier

Synopsis: This ToC graphic outlines the main ideas presented in the manuscript. The image on the left is generated by different sizes and arrangements silicon disks as mentioned in the manuscript, with different sizes corresponding to different color observed. The SEM image has shown the silicon disk on aluminum from top view. Below the SEM image, we plotted the 3D perspective schematics of the structures used. On the right side of the ToC graphic, we outline the concept of the method of images and we wrote down the key results derived to generalize the method of images to multipolar scatterings.